Additive Manufacturing 28 (2019) 236–251

Contents lists available at ScienceDirect

Additive Manufacturing

journal homepage: www.elsevier.com/locate/addma

Spatially resolved acoustic spectroscopy for integrity assessment in wire–arc additive manufacturing

Paul Dryburgh[a,b,*], Don Pieris[a,b], Filomeno Martina[c], Rikesh Patel[a], Steve Sharples[a], Wenqi Li[a], Adam T. Clare[b], Stewart Williams[c], Richard J. Smith[a]

[a] Optics and Photonics Group, University of Nottingham, University Park, Nottingham NG7 2RD, UK
[b] Advanced Component Engineering Laboratory, University of Nottingham, Jubilee Campus, Nottingham NG8 1BB, UK
[c] Welding Engineering and Laser Processing Centre (WELPC), Building 46, Cranfield University, MK43 0AL, UK

ARTICLE INFO

Keywords:
Additive manufacturing
Ultrasonic inspection
Titanium
Grain refinement
Crystallographic texture

ABSTRACT

Wire–arc additive manufacturing (WAAM) is an emergent method for the production and repair of high value components. Introduction of plastic strain by inter-pass rolling has been shown to produce grain refinement and improve mechanical properties, however suitable quality control techniques are required to demonstrate the refinement non-destructively. This work proposes a method for rapid microstructural assessment of Ti–6Al–4V, with limited intervention, by measuring an acoustic wave generated on the surface of the specimens. Specifically, undeformed and rolled specimens have been analysed by spatially resolved acoustic spectroscopy (SRAS), allowing the efficacy of the rolling process to be observed in velocity maps. The work has three primary outcomes (i) differentiation of texture due to rolling force, (ii) understanding the acoustic wave velocity response in the textured material including the underlying crystallography, (iii) extraction of an additional build metric such as layer height from acoustic maps and further useful material information such as minimum stiffness direction. Variations in acoustic response due to grain refinement and crystallographic orientation have been explored. It has been found that the limited α-variants which develop within prior-β grains lead to distinctive acoustic slowness surfaces. This allowed prior-β grains to be resolved. A basic algorithm has been proposed for the automated measurement, which could be used for in-line closed loop control. The practicality and challenges of applying this approach in-line with fabrication are also discussed.

1. Introduction

Additive manufacturing (AM) promises to herald a new age in fabrication, by improving utilisation of raw materials and removing many of the design constraints found with traditional techniques. A form of this, known as wire–arc additive manufacturing (WAAM), uses a wire feedstock and welding arc, to build up multiple layer structures [1], *see* Fig. 1 [2]. In comparison to powder-bed fusion, WAAM is able to produce larger parts at significantly faster deposition rates, up to 10 kg/h compared to 50–200 g/h [3]. However, these techniques generally cannot produce the intricate featuring seen in powder-bed fusion, making WAAM well suited to less complex, large build-volume components [2]. The main drivers for WAAM's adoption are reduction in manufacturing cost thanks to reduced waste; and reduction in lead times [4].

Ti–6Al–4V is an α + β titanium alloy, favoured thanks to its high strength-to-weight ratio and good corrosion resistance; this gives it uses in aerospace, pressure vessels, gas turbines and surgical implants [5]. The high processing temperatures found in WAAM promotes the formation of prior-β grains at high temperatures, before rapid cooling to form α′, and α in a Widmanstätten pattern [6,7]. Burgers orientation relationship defines the transformation between the high temperature cubic β-phase and the low temperature hexagonal α-phase, given in Eq. (1). This allows 12 α orientations to form within a prior-β grain [8].

$$\{110\}_\beta // (0001)_\alpha \quad \langle 111\rangle_\beta // \langle 2\bar{1}\bar{1}0\rangle_\alpha \tag{1}$$

In practice, for a known orientation of the parent β-phase, g^β, the twelve possible α-variants can be predicted by Eq. (2). This process has been explained in detail by Davis [9].

$$S_j^\alpha \mathrm{DS}_1^\beta g^\beta,\ \ldots, S_j^\alpha \mathrm{DS}_i^\beta g^\beta,\ \ldots, S_j^\alpha \mathrm{DS}_{12}^\beta g^\beta \tag{2}$$

where S^ψ is the symmetry rotation, for α (hexagonal) or β (cubic) phases, and D is the rotation corresponding to the Burgers orientation relationship. The symmetry rotation matrices were introduced by

* Corresponding author at: Optics and Photonics Group, University of Nottingham, University Park, Nottingham NG7 2RD, UK.
E-mail address: paul.dryburgh@nottingham.ac.uk (P. Dryburgh).

https://doi.org/10.1016/j.addma.2019.04.015
Received 13 March 2019; Received in revised form 18 April 2019; Accepted 21 April 2019

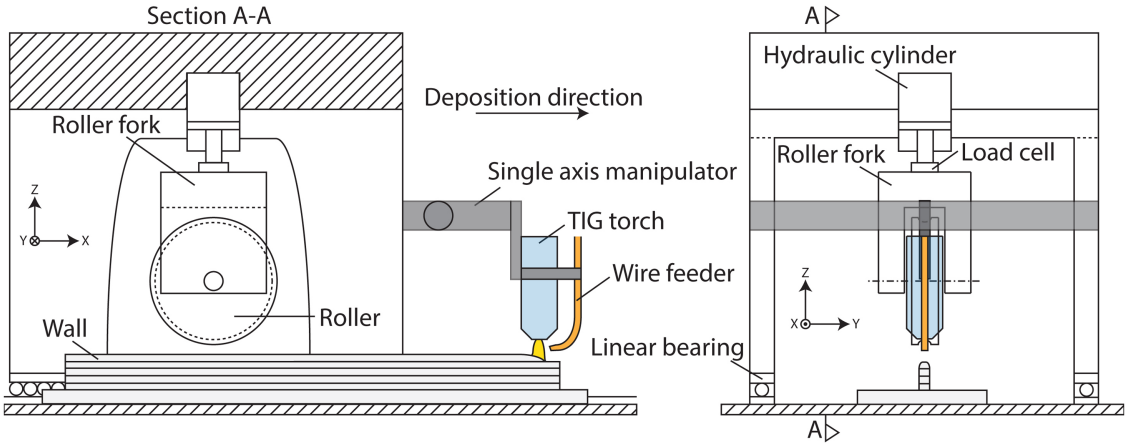

Fig. 1. Diagram of automated welding equipment used in WAAM, as used to fabricate the specimens analysed in this study [31].

Humbert et al. in their explanation of reduced numbers of orientation variants in phase transition [10]. This limited number of orientation possibilities leads to large microtextured regions, much larger than the size of the individual α-phase grains [11]. Sinha et al. showed that the crystallographic orientation and size of the large microtextured regions are associated with facet-initiation sites of fatigue cracks [12].

Components manufactured by an additive process are characterised by a strongly anisotropic microstructure, primarily columnar grain growth in the build direction [13]. In WAAM processed Ti–6Al–4V this leads to < 001 > alignment in columnar prior-β grains, and this gives rise to strong texturing of the child α grains [14]. This is known to contribute to mechanical anisotropy [15], inferior fatigue life [16], geometric distortion and crack initiation at prior-β grain boundaries [17]. Martin et al. have suggested that one way of producing a microstructure more suitable to engineering applications and preventing the induced residual stress is to promote equiaxed grain growth [18]. The use of inter-pass rolling has also been trialled in WAAM to induce plastic strain to relieve tensile stresses and enact grain refinement [19,20]. This approach was found to significantly reduce the prior-β grain size and weaken the texture of both the prior-β and final α structures [21,14]. The resulting texture leads to components with more isotropic properties.

To date, a lack of well suited validation techniques has been cited as one of the greatest inhibitors to the industrial pick-up of AM [22]. Development of in-line monitoring techniques for directed energy deposition methods have primarily focused on optical and thermal methods, with a view to control of the build geometry, with little work on microstructure or defect detection being reported [23]. Recent literature focused on the industrialisation of WAAM has shown that the effectiveness of the rolling process is dependent upon the roller's geometry, as well as the rolling strategy, rolling load and/or the spacing between adjacent rolling passes [24]. An in-line technique to monitor grain refinement would allow for closed-loop control of the rolling force, minimise parameter optimisation time and, crucially, enable quality control facilitating the industrialisation of WAAM.

Currently, inspection of the microstructure of Ti alloys requires the specimen to be sectioned and prepared for diffraction techniques such electron backscatter diffraction (EBSD) or through etching and microscopy. Neither option can be applied in-line with the WAAM process non-destructively.

This study presents an all-optical monitoring technique using laser induced ultrasound, known as spatially resolved acoustic spectroscopy (SRAS), for rapid texture assessment in WAAM components. SRAS is a non-contact, non-destructive evaluation technique which probes the elastic properties of materials using surface acoustic waves (SAW). The technique and instrumentation have been reported at length in previous literature and applied to PBF [25,26].

Farnell first reported the crystallographic orientation dependence of SAW velocity [27]. This angular dependency was exploited by Li et al. for the calculation of crystallographic orientation by SAW velocity measurement in large grain industrially relevant alloys and pure metals [25,26]. More recently, SRAS has been suggested as a tool well suited to address many of the challenges of quality control in powder-bed AM. This can be summarised as SRAS' ability to detect and differentiate surface and subsurface defects [28], capability to characterise meso-scale microstructure features of the specimen [29] and be used as a tool to inform remedial action [30]. To date, the effects of dual-phase materials on SRAS imaging have not been reported. In effect, as the α-phase is probed, it is unclear if features from the prior-β grains can be captured.

This study utilises the SRAS technique to capture SAW velocity maps from undeformed and rolled WAAM specimens, in both polished and as-deposited states. The three primary aims of this work are:

- Understand the extent to which the texture and other features originating from the fabrication process can be probed through the use of SAWs.
- Investigate if SAW velocity maps can be used to measure the efficacy of rolling.
- Establish the feasibility of capturing these measurements in-line, as a step towards inspection during fabrication.

This work demonstrates off-line inspection of prepared WAAM fabricated specimens using SRAS. The detection of prior-β grains and the microstructural differentiation between undeformed and rolled specimens has been successful, and explanation to relate the underlying microstructure to the measured acoustic response has been provided. Further investigation of the angular response allows the anisotropic features to be studied, which has been utilised to extract further information such as the texture of the substrate and minimum stiffness direction. Finally, the challenges to overcome for on-line inspection are explored in detail.

2. Materials and methods

2.1. WAAM specimens

All specimens reported in this study haven been produced using the WAAM process using Ti–6Al–4V welding wire feedstock, on to a titanium substrate. A pulsed gas tungsten arc welding torch, with argon shielding, was used to deposit structures made of 20 single-bead layers, giving an approximate final width of ~6mm and height of ~24 mm. Following the deposition and cooling of each layer, a 100 mm diameter roller was passed over the top surface to create the deformed

Table 1
WAAM deposition parameters, used to fabricate specimens for this study.

Build parameter	Value	Unit
Average arc voltage	12	V
Average current	110	A
Peak current	150	A
Background current	70	A
Frequency	10	Hz
Torch stand-off	3.5	mm
Torch shield gas flow rate	10	$l\,min^{-1}$
Trailing gas flow rate	20	$l\,min^{-1}$
Travel speed	270	$mm\,min^{-1}$
Wire diameter	1.2	mm
Wire feed speed	1.6	$m\,min^{-1}$

specimens. Rolling applied vertical forces were of 50 or 75 kN, monitored by a load-cell, as shown in Fig. 1. Key build parameters are given in Table 1 and further detailed information on the WAAM process can be found in Martina et al. [2].

Specimens were sectioned using electrical discharge machining and mounted. For each roller force, both the x–z and y–z planes were exposed for analysis. All specimens were prepared by standard metallographic preparation for titanium, and etched with Kroll's reagent for optical micrographs. Additionally, sections of the undeformed and 75 kN rolled specimen have been left unprepared so as to allow imaging in the as-deposited state to simulate measurements performed in an industrial environment during the manufacture of a component.

2.2. Microstructure analysis and preparation

To establish a baseline of specimen microstructure, EBSD orientation images were captured using a JEOL 7100F FEG-SEM scanning electron microscope, with an Oxford Instruments EBSD system and Aztec acquisition package. The MATLAB package MTex was used for processing and preparation of pole figures, with a 5×5 median window used to smooth the collected EBSD data. Representative optical macrographs were captured using a Leica M205 FA stereo microscope and stitched together in post-processing. Finally, high resolution images and surface profiles of the as-deposited side-walls have been captured with a focus variation microscope, Alicona InfiniteFocus G5, with $10\times$ objective lens, giving a lateral resolution of 3.9 µm.

2.3. Spatially resolved acoustic spectroscopy

In brief, the use of an optical mask with known grating spacing, λ_g, imaged as a fringe patch onto the specimen surface, allowing the temporal frequency of the pulsed laser and the spatial frequency of the specimen to be matched. Through thermo-elastic absorption of the pulsed laser energy acoustic waves were generated in the specimen. As the specimen thickness is much greater than the inspection wavelength Rayleigh Surface Acoustic Waves (SAWs) were generated, and propagated with a frequency f_s. The non-dispersive nature of Rayleigh waves meant this characteristic frequency stayed constant, allowing detection at an arbitrary distance from the generation patch.

A secondary laser was used to probe the frequency, f_s, of surface perturbation caused by propagation of the SAW packet, by a knife-edge detector (KED). Thus, the SAW velocity was determined by Equation

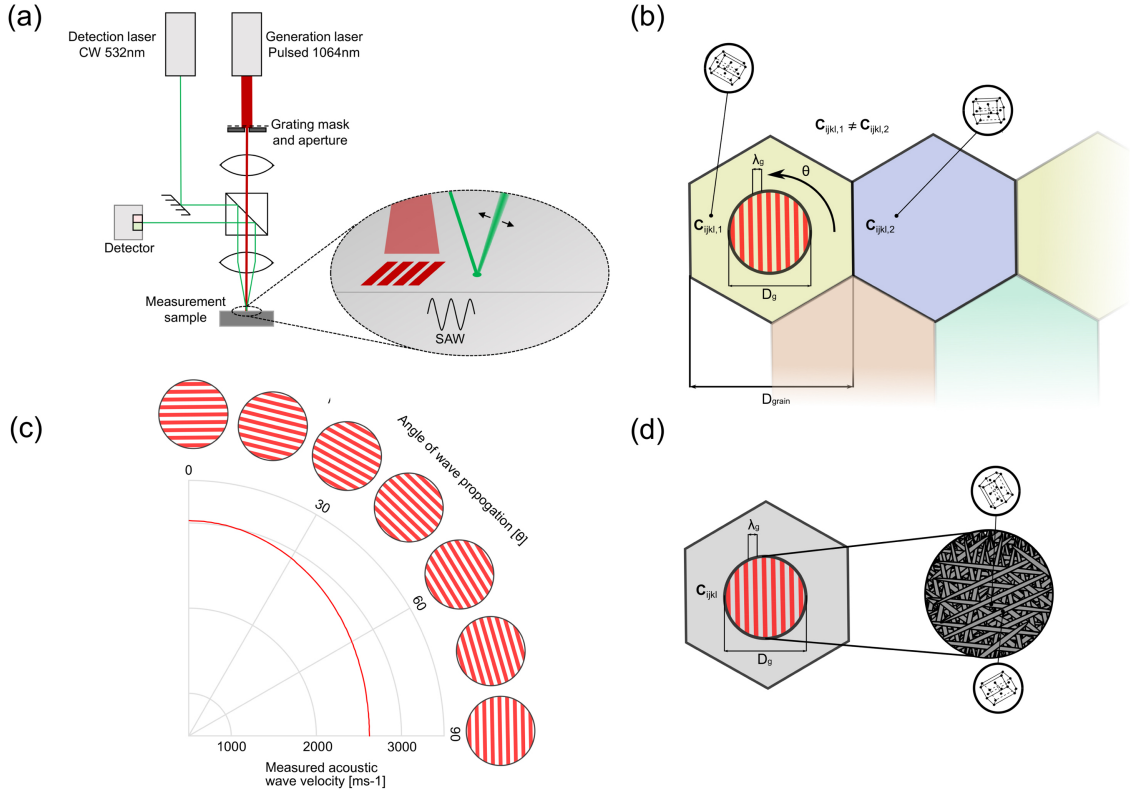

Fig. 2. (a) Schematic of spatially resolved acoustic spectroscopy set-up, showing excitation and detection of a SAW in a specimen by surface perturbation, and corresponding optical path. (b) Normal SRAS experiment in large grain materials, five grains of different stiffness shown in this diagram, where the generation patch, D_g is much smaller than the grain, $D_g$rain. In specimen like this the orientation of each grain region can be found. (c) The measured SAW velocity is a function of wave propagation angle, θ. The shown slowness surfaces shows a typical variation in titanium between 0 and 90 degrees of $\sim 300\,ms^{-1}$. (d) Diagram of SRAS experiment in specimen with fine Widmanstätten pattern; at each fringe the acoustic wave velocity is a function of the elastic properties of all lamella, C_{ijkl}, in that fringe width, λ_g. It is possible to have acoustic impedance mismatch due to differing crystal orientations.

(3), through measurement of the characteristic frequency of the wave packet.

$$v_{saw} = f_s \lambda_g \quad (3)$$

The velocity of these SAWs, v_{saw} is a function of the elastic properties of the specimen, furthermore, the calculated velocity is a property of the specimen area under the generation patch only. This makes SRAS robust to scattering and aberration effects induced from microstructure which plague traditional ultrasonic time-of-flight methods. The current iteration of SRAS instrumentation (schematic shown in Fig. 2) uses a broadband Q-switched laser (AOT-YAG-10Q), at a wavelength of 1064 nm (near-infrared) for generation. The laser operates at a repetition rate of 2 kHz, with a pulse width of 1–2 ns and pulse energy of 50–150 μJ. The detection laser is a Cobolt Samba, with wavelength 532 nm (green) continuous wave laser with an output of 200 mW, after fibre coupling into the optical set-up. Scanning stages (Physik Instrumente M-413 and M-414) were used to keep the optical set-up static and move the specimen for raster scanning. All SRAS data presented in this work was captured with an acoustic wavelength of 24 μm, with a generation patch diameter of 200 μm, leading to an approximate spatial resolution of 100 μm [26]. Datasets were captured at various source detector rotations between 0 and 170°, allowing the texture anisotropy to be evaluated.

In large grain materials [32] where the acoustic wavelength $\lambda_g << D_{grain}$ (where D_{grain} is the major axis length of the grain), each measurement point can be treated as a single crystal, Fig. 2(b). The angular response of such grains, Fig. 2(c) is well understood. However, in fine micro structures such as WAAM processed Ti–6Al–4V, where $\lambda_g >> D_{grain}$, the acoustic velocity is a function of the elastic properties of all lamella in that fringe width, as shown in Fig. 2(d). When generating across multiple orientations or phases, the measured wave packet contained multiple frequency components. The measured velocity by the SRAS technique was then the most common SAW frequency within the whole generation patch, selected by taking the maximum amplitude in the frequency domain. Increasing the number of phases or orientations under the generation patch will increase the bandwidth of the signal, decreasing the velocity resolution and signal-to-noise ratio.

Various schemes exist for estimating the bulk elastic properties of anisotropic polycrystalline materials, the most common of which is the Voigt-Reuss–Hill approximation. Using the texture distribution obtained by EBSD, the stiffness tensor for the hexagonal α-phase was transformed into the orthorhombic macroscopic tensor. This allowed a prediction of the SAW velocity, as measured by the SRAS technique, when generating across a region with many dissimilar grain orientations. A full introduction to the Voigt-Reuss-Hill method and its application to SAWs can be found in Kube et al. [33].

3. Results

3.1. Side-wall measurements (x–z plane)

Acoustic velocity maps captured with SRAS for varying rolling force are shown in Fig. 3, for the (a) undeformed and (b) 75 kN rolled specimens respectively, after polishing. All specimens are orientated as shown by Fig. 1.

Considering first the undeformed specimen, Fig. 3(a), columnar structuring, running the length of the specimen in the *z*-direction and around 2–3 mm in width, can be discerned in the acoustic image. These large features are consistent with the formation of prior-β grains. Within the prior-β grains themselves, there is little acoustic variation; this is representative of large microtextured regions. For a single grain the velocity varies with crystallographic orientation by ± 250 ms^{-1} for Ti–6Al–4V; the observed variation is lower as the average velocity is measured for the grain population underneath the patch. However, velocity variations of ~ 100 ms^{-1} can be seen between prior-β grains. A band of ~ 500 μm in height can be seen at the very top of the specimen; this represents the final deposited layer, which has not had the opportunity to recrystallise from subsequent deposition. Grain growth is found to be at a mean angle of 74.2° ± 2.2° to the *x*-direction, as indicted by the dashed lines in Fig. 3(a). This 16° rotation from ideal vertical growth is caused by the direction of deposition (left to right), creating a thermal gradient in the *x*-direction. This is consistent with the findings of Donoghue et al. [14].

Fig. 3(b), shows the acoustic velocity map for the 75 kN rolled specimen. No columnar structuring can be discerned, suggesting the acoustic response has detected the effects of inter-pass rolling. There is no larger scale structuring, of millimetre scale, but significant velocity variations can be seen across the specimen. This suggests a more equiaxed microstructure, with a more varied microstructural texture. The velocity variations occur in a spatial range of hundreds of micrometers, compared to millimetres in the undeformed specimen, consistent with a refined β-grain size.

For comparison an enlarged macrograph, after etching, taken from the 75 kN rolled specimen is shown in Fig. 3(c). There is good agreement between structure shown in the SRAS velocity map and the etched image. The macro-regions shown are consistent with the formation of prior-β grains, which in the rolled specimens do not have a fibre texture. Dashed lines indicate representative macro-structure features which can be seen in both Fig. 6(b) and (c).

3.1.1. Angle dependent response

Acoustic maps have also been captured at varying source rotations in order to probe possible anisotropic effects. SRAS velocity maps for acoustic propagation angles of 0, 45 and 90° for the three prepared side-wall specimens are shown in Fig. 4(a)–(i). Again, a clear distinction can be drawn between the undeformed and rolled specimens; whilst the rolled specimens show little angle dependency, the undeformed specimen exhibits variations of up to 100 ms^{-1}. For example, in the 0° map there is little contrast between prior-β phases, however in the 90° map a variation of around 100 ms^{-1} can be seen between prior-β grains. This is suggestive of close crystallographic alignment between prior-β grains in the *z*-direction, and misalignment in the *x*-direction. A variation of ~ 100 ms^{-1} due to varying propagation angle is suggestive of anisotropic elasticity, typical of large microtextured regions.

Additional features are revealed in the angle scans, such as the high velocity response that runs as a line from the top left of the specimen to the bottom in the 45° scan, Fig. 4(b). Interestingly, some prior-β grains are seen to split off as the deposition continues, triggered by the formation of thinner grains within. A repetitive banding can be seen in the *z*-direction; this likely corresponds to the layers of deposition. This feature is most clear in the 90° scan, because the axial resolution is normally significantly better than the lateral resolution due to the nature of the generation patch in SRAS [26].

In both the 0 and 45° degree scan in the undeformed specimen high velocity regions are seen at the interface between some of the prior-β grains. From inspection of the measured acoustic waves, this effect is believed to be an anomalous velocity caused by significant acoustic impedance mismatch between the prior-β grains, causing reflection of the acoustic wave across the generation patch, convoluting the final measurement in a small area. This effect will only be noticed in areas of high β-phase concentrations.

Clearly from these maps the prior-β features can be discerned, an interesting outcome as the acoustic measurement is probing the α-phase. The acoustic response throughout these prior-β features appears consistent. Of further interest is the inconsistency of the anisotropy of the prior-β grains. For example, in the undeformed specimen some prior-β show no measurable acoustic variation with propagation angle.

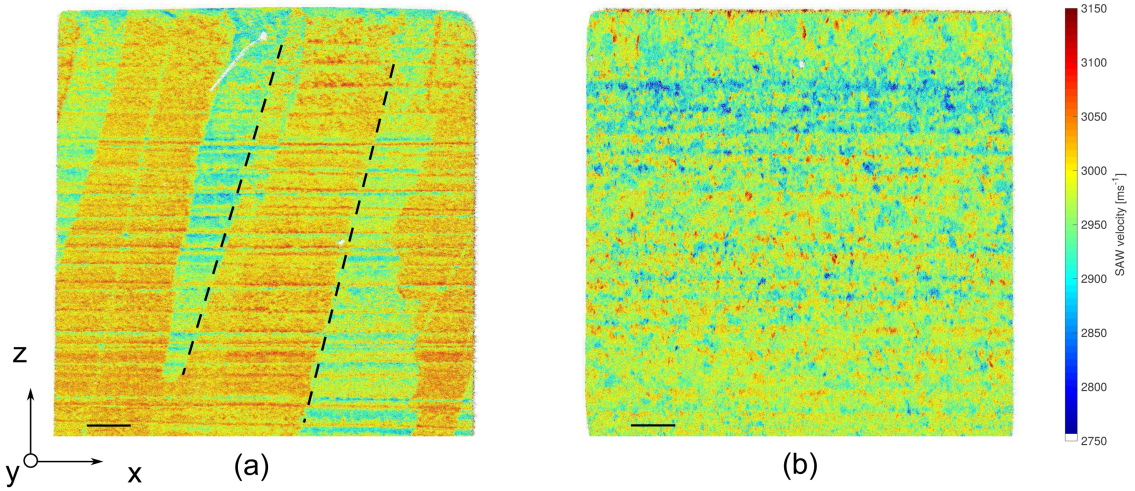

Fig. 3. Results from prepared side-wall (x–z). Scale bars indicates 2 mm. (a) SRAS velocity map from undeformed specimen, annotated lines have been added to indicate vertical prior-β grain growth. (b) SRAS velocity map from 75 kN rolled specimen, large prior-β features can no longer be discerned.

3.2. Cross-section measurements (y–z plane)

Additional SRAS maps have been captured from the prepared cross-section, y–z plane in the undeformed and 75 kN rolled specimens. Results are shown in Fig. 5. An etched macrograph of the undeformed cross-section is shown Fig. 5(a) and the corresponding SRAS acoustic map in Fig. 5(d). Acoustic maps for this specimen were captured at propagation angles of 0–170°, in 10° increments. Please note the map shown is from 110°.

The most prominent feature seen in the SRAS velocity map Fig. 5(d), is the region in the lower left of maximum 6 mm in height, which extends across the specimen at $\sim 150\,\mathrm{ms}^{-1}$ slower than the bulk of the specimen. Inspection of the macrograph, Fig. 5(a), shows clear parallels with the acoustic map Fig. 5(d), foremost the low velocity region can be clearly seen in both images. Again, this is attributed to the formation of a prior-β grain.

To further understand the interface between the regions, a detailed micrograph at the boundary is shown in Fig. 5(c). The etched surface reveals a typical α + β microstructure, with a clear interface running diagonally. α-phase lathes can be seen on either side of the interface but at a different orientation. The interface observed optically (i) agrees well with the boundary seen in the SRAS velocity map, and is consistent with the formation of misorientated prior-β grains. For comparison a similar micrograph has been captured toward the top of the specimen Fig. 5(b), where no acoustic boundary can be seen, this region is the final layer of deposition which has not been reheated (iv). In line with this, a consistent Widmanstätten pattern is seen with no substantial change in orientation.(ii) Boundaries between deposited layers are again observed. (iii) Close inspection of the etched image, also shows repeated curved bands which correspond to the fusion boundary segregation band, these features are also weakly seen in the acoustic map. Ho et al. have shown these bands are caused by the development of a transient solute boundary layer at the solidification front when it first accelerates, causing chemical segregation [7]. Such a change in chemical composition explains why this region can be discerned in the acoustic map.

The y–z cross-section of the 75 kN specimen has also been prepared and scanned, Fig. 5(e) shows the acoustic velocity map from a propagation angle of 90°. Notably, the distortion of the build in the direction can clearly be seen. Whilst little structuring can be seen towards the centre of the specimen, in-line with significant grain refinement, larger features (up to 2 mm in length) are observed towards the edge of the specimen. This is indicative of the strain field induced by the roller not being evenly distributed though the specimen; indeed, grain refinement is more efficacious towards the centre of the cross-section. The boundaries due to layer deposition are again seen.

3.3. Examination of interface

In WAAM, the layer-wise deposits are built up from a substrate; for titanium alloys an annealed α + β titanium base is used. Fig. 6 shows the acoustic velocity maps for the interface between the substrate and the deposited structure at propagation angles of 0, 45 and 90° Fig. 6(a)–(c), captured at the area indicated in the extended 0° velocity map, Fig. 6(d). Firstly, it is clear that texture is much more homogeneous in this area directly above the substrate, suggesting a finer grain size in this region. As this effect occurs only in this isolated area, it is likely to due to the heat sink effect of the substrate causing rapid cooling of the deposition, preventing epitaxial grain growth. Compared to the substrate, the deposited area near the interface shows little acoustic variation, either within a single scan or at varying propagation angles, Fig. 6(b)–(d). The little contrast seen suggests the texture is consistent across this region of deposition. Furthermore, the measured velocity is around $50\,\mathrm{ms}^{-1}$ away from the calculated mean velocity, suggesting there is a strong non-random texture in this region.

One additional result that may be of interest is the acoustic response of the substrate. From Fig. 6(b)–(d), variations of up to $250\,\mathrm{ms}^{-1}$ in the acoustic response suggest crystallographic anisotropy. Fig. 6 shows a velocity vector map for the substrate area, which amalgamates the 0 and 90° scans to show the alignment of the c-axis in large grain hexagonal materials [26]. In this instance, the vector map Fig. 6(e) suggests a strong aliment with the prism plane (basal plane in x-axis).

Finally, some texture inheritance can be seen to propagate from the substrate into the initial few layers of the deposition, in the order of tens of micrometres. Given previous investigations have shown that the orientation of the substrate influences the orientation developed in the additive part [34], the substrate texture may be important for control of the deposition in future. Donoghue et al. described the 'ratcheting process' that occurs in the undeformed WAAM specimens where by, in situations where rolling is not applied the original β-grains simply regrow the orientations of the substrate during epitaxial solidification of the next layer deposited. Therefore, in situations where rolling is not applied, knowledge of the original orientation of the substrate may be crucial for control of the large prior-β structures.

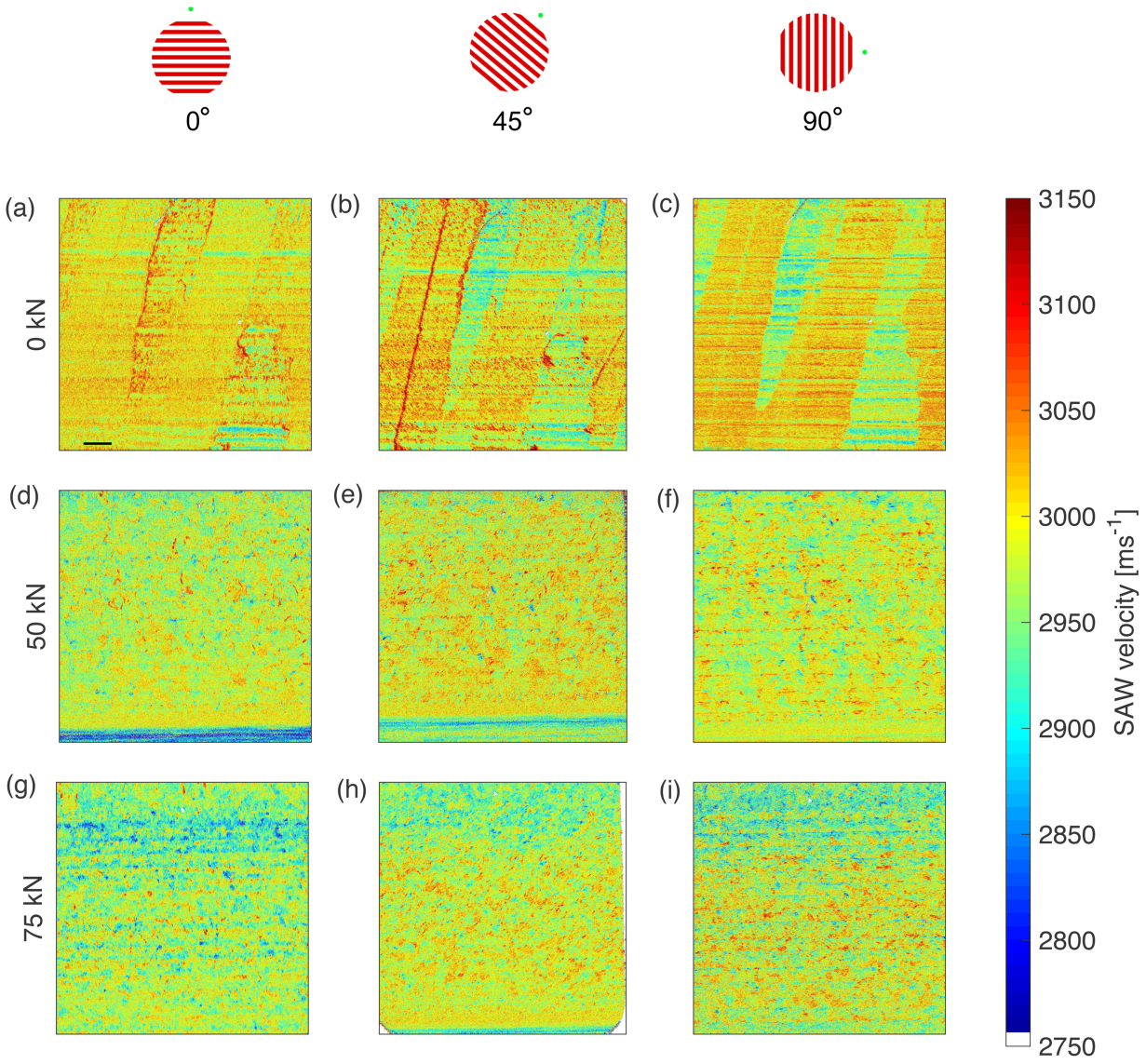

Fig. 4. Varying the propagation direction of the SAW, by rotation of the optical mask and detection spot – as illustrated at the top of the figure, relative to the specimen allows the effects of material anisotropy to be probed. SRAS acoustic velocity maps captured for three WAAM specimens (a)–(c) undeformed, (d)–(f) 50 kN, (g)–(i) 75 kN rolling force, for propagation angles of 0, 45 and 90°, relative to the *z*-axis, as indicated by fringe schematics at the top of figure. Scale bar shown in (a) applies to all figures and indicates 2 mm.

4. Discussion

4.1. Crystallography

The captured velocity maps describe the acoustic response of the α-phase, thus it is interesting that prior-β grains can still be discerned. As discussed, the fine lathe size found in the α-phase prevents direct recovery of the crystalline orientation, but several conclusions may still be drawn on the crystallography of the WAAM depositions. Fig. 7 defines the hexagonal α-phase crystal, and Euler–Bunge rotation notation that will be referenced throughout this section.

In previous work by Donoghue et al. [14], recovery of the prior-β macrostructure from EBSD imaging, revealed a repeating orientation of columnar grains along the *x*-direction. This is demonstrated in Fig. 7, (b) hexagonal phase inverse pole figure and (c) reconstructed cubic phase inverse pole figure. In Fig. 7(b) clear columnar growth at an angle similar to that presented in acoustic map in Fig. 3. Furthermore, the orientation of grains can be seen to alternate between an orientation of [001] and one closer to [101], demonstrated by grains indicated by (i) and (ii). Observation of the SRAS data suggests a similar repeating pattern in the columnar growth, along the x-direction. This patterns appears more obviously in the SRAS due to the stark velocity contrast in the 90° scan between prior-β grains. This suggests that the acoustic variation between prior-β grains, seen in Fig. 4, is due to changes in orientation of the prior-β grains.

The general approach taken in this section has been summarised by the block diagram shown in Fig. 8. EBSD data has been captured for all prepared side-wall specimens imaged in this study. Due to the orientation variants possible in the α-phase, direct interpretation of the inverse pole figures is challenging. The texture distribution is more clearly seen by considering the respective pole figures, Fig. 9, for each specimen. The undeformed specimen Fig. 9(a) shows a strong texture in the (0001) plane, comparatively the 50 kN specimen shows a weaker texture, primarily in the (0001) plane but also observable in the $(11\bar{2}0)$ plane. This is consistent with a greater variety of α-phase orientations, due to the break-up of prior-β grains.

Results from Section 3.1.1 suggested the angular dependence on SAW velocity varied between the three specimens. To compare this

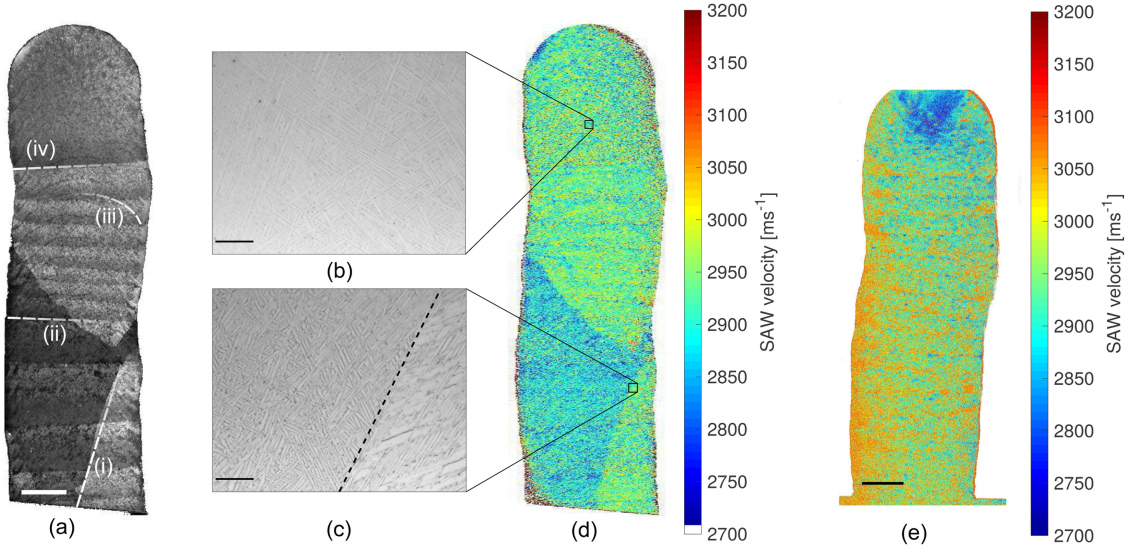

Fig. 5. Results from *y*–*z* plane cross-section specimens, (a)–(d) undeformed specimen (e)–(f) 75 kN rolled specimen. (a) Etched macrograph, (i) showing prior-β formation, (ii) interface at layers of deposition, (iii) fusion boundary and (iv) final deposited layer which has not been reheated. (b) and (c) Micrographs taken after etching scale bar indicates 250 μm, (c) shows the interface between two prior-β grains. (d) SRAS velocity map corresponding to (a). (e) 45° SRAS velocity map from 75 kN rolled specimen and (f) 90° SRAS velocity map from 75 kN rolled specimen. All Scale bars indicates 2 mm, except in (b) and (c).

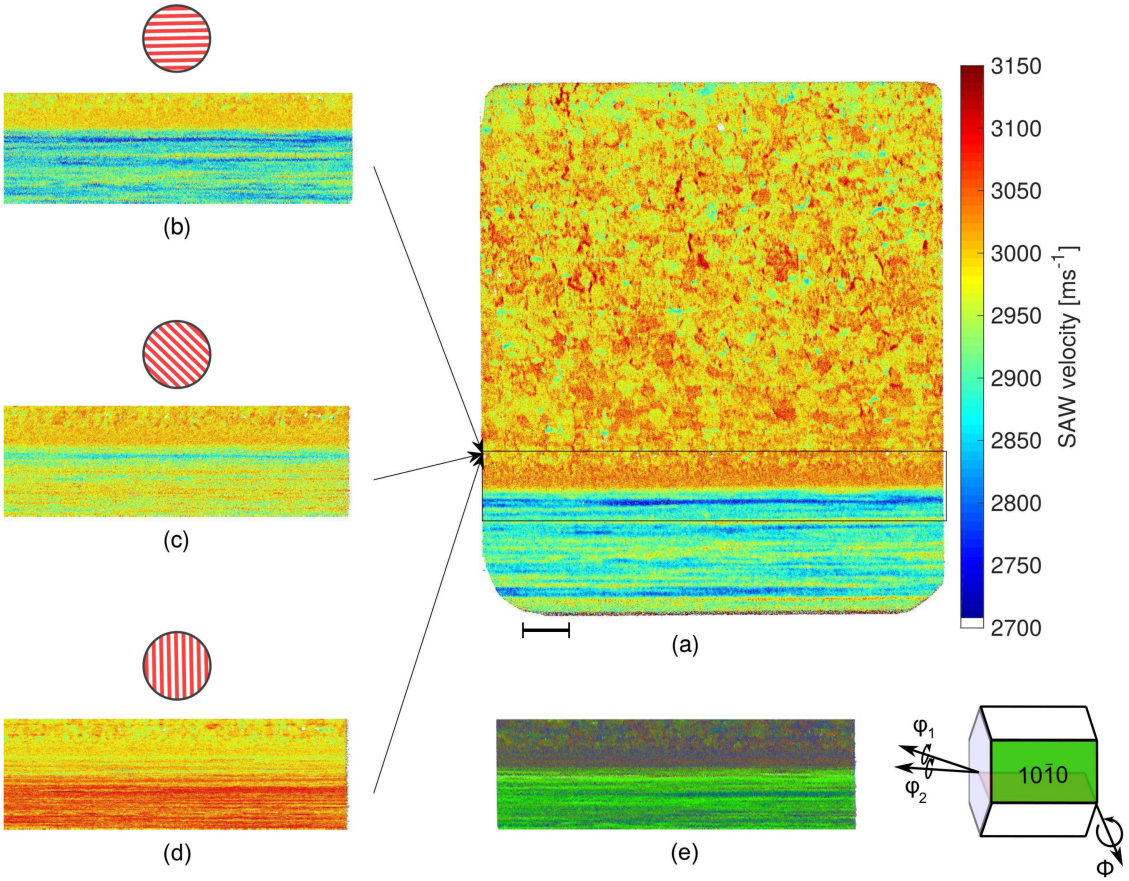

Fig. 6. SRAS is able to map the texture of the substrate as well as the deposition. (a) Shows the full SRAS velocity map from the 50 kN rolled specimen, captured at 0°, the indicated area represented the interface between the deposition and substrate. Magnified velocity maps of this interface are given in (b)–(d) at propagation angles of 0, 45 and 90°, respectively. There is a clear grain refinement in the deposition. Strong anisotropic response from the substrate. (e) Shows the corresponding vector map for the substrate area, this map indicates the dominant alignment of hexagonal crystals with respect to the *c*-axis. Whilst no clear preference can be seen in the deposition, there is a clear preference towards the prism plane (ϕ_1 close to 0°), due to insensitivity to ϕ_2 this plane may be $\{10\bar{1}0\}$ or $\{11\bar{2}0\}$. Scale bar indicates 2 mm.

quantitatively, Fig. 10 plots the change in velocity at each measurement point between the 0 and 90° propagation direction scans. In the undeformed specimen Fig. 10(a) prior-β grains are clearly seen, with a variation of up to 100 ms^{-1}. Within the prior-β grains themselves there is little acoustic contrast, less than 40 ms^{-1}. This is a useful property for the identification of unrefined microstructure acoustically. Whilst

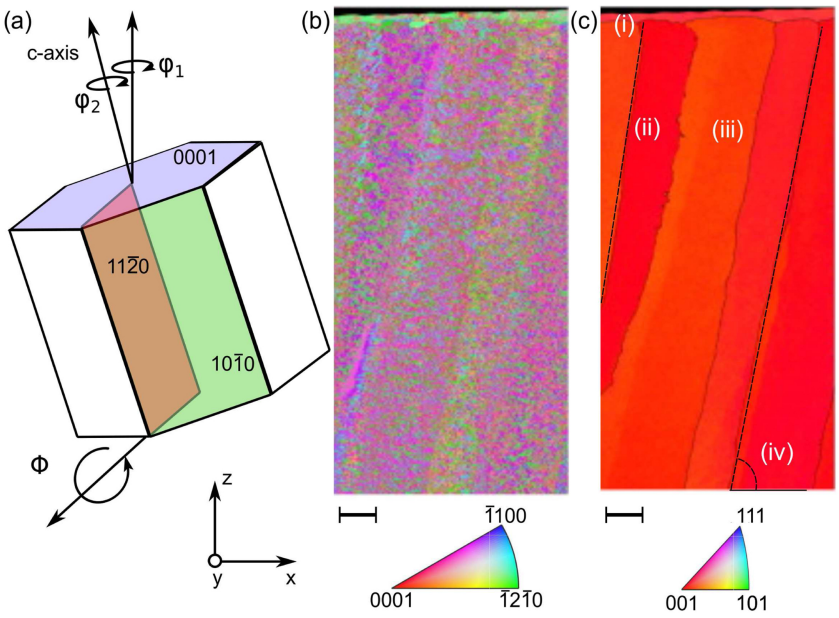

Fig. 7. (a) Definition of axis and planes in reference to α-phase hexagonal crystal, as given by Euler–Bunge notation. Vector map plot shown in Fig. 6 is relative to the *c*-axis direction. Linear acoustic techniques are insensitive to variations in ϕ_2 [32], due to elastic transverse isotropy. In practice, this limits the ability to differentiate between (11$\bar{2}$0) and (10$\bar{1}$0) planes [32]. (b) and (c) Measured hexagonal phase and corresponding reconstructed cubic β-phase inverse pole figures, captured using EBSD by Donoghue et al. courtesy of Materials Characterization © 2016. Scale bars indicate 1 mm. (b) (i) Microstructrual segregation at the top of the specimen, corresponding to the final layer of deposition. (ii) and (iii) Repeating pattern in prior-β orientation. (iv) Clear columnar growth can be seen at a similar angle to that shown in Fig. 3.

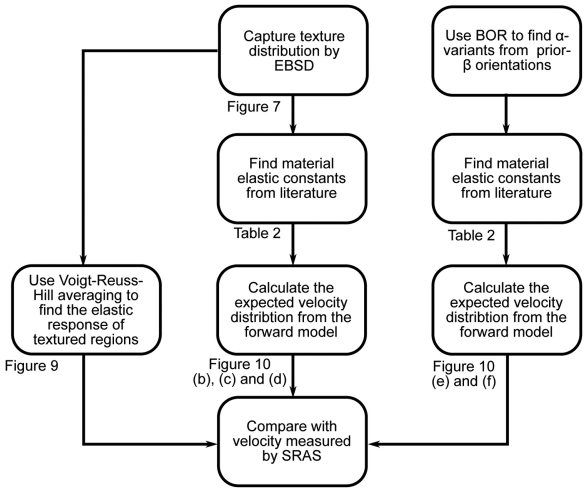

Fig. 8. Block diagram of methods utilised in this section to understand the crystallography and texture development in the probed WAAM specimens, with respect to the SAW velocity information captured by SRAS in Section 3.

angular variations are seen in both the Fig. 10(b) 50 kN and Fig. 10(c) 75 kN rolled specimens, there are much more in the 75 kN sample and on a smaller scale. Given that 75 kN specimen has the finest prior-β size, this suggests the contrast feature size shown in Fig. 10(b) and (c) are representative of the size of prior-β grains. Additionally, the frequency of angular acoustic velocity contrast appears to be related to the efficacy of grain refinement.

From comparison with the work of Donoghue et al. it has been established that the acoustic contrast between prior-β grains is due to a change in orientation of the prior-β grains. However, this does not explain the limited acoustic variation seen within a prior-β grain or why some exhibit a greater angular dependency than others, as observed in both the undeformed and rolled specimens as in Fig. 10. To look at this further the measured EBSD data has been used to predict the macroscopic elastic tensor of the measured specimen. It should be noted that the EBSD from the undeformed specimen was captured fully within a prior-β grain showing significant acoustic variation with propagation direction. Given the small feature size in the rolled specimens it is not possible to know how many prior-β grains are captured within these EBSD datasets. Firstly, having captured the EBSD data it was then possible to combine this with the previously described Voigt-Reuss-Hill method, for calculation of the average elastic tensor. The initial hexagonal tensor is defined in Table 2. The resulting tensor has triclinic crystal symmetry, and given the dependency of SAW velocity on stiffness it is of interest to plot the Young's modulus as a function of direction. Fig. 11 shows the averaged Young's modulus for the three prepared (*x*–*z*) side-wall specimens, calculated using the Hill method from the EBSD data shown in Fig. 9. The Hill method is an arithmetic average of the upper and lower bounds given by the Reuss and Voigt methods.

This plot exhibits the anisotropic behaviour of the undeformed specimen, as seen in the angular acoustic response, Fig. 4. The shift of ~ 4 GPa in the undeformed specimen would correspond to a shift of over 50 ms^{-1} in SAW velocity, this compares well with the change in velocity seen in Fig. 10(a). In contrast, the rolled specimens exhibit a much smaller stiffness variation and thus smaller angular velocity change, this again matches well with the results of Fig. 4, to within 25 ms^{-1}, which compares well with the accuracy suggested by Kube et al. for the prediction of acoustic wave velocity from the Hill method [33]. Both rolled specimens have a maximum change in Young's modulus of 1 GPa, corresponding to a variation in SAW velocity of around 15 ms^{-1}. This compares with the response from the 50 kN rolled specimen (Fig. 10(b)); however, the 75 kN rolled specimen appears to exhibit large velocity contrasts in small regions, more notable towards the top of the specimen. These small regions are likely to correlate to the refined prior-β grain size, the EBSD data from the 75 kN rolled specimen is captured from a region with low velocity variation, which agrees with the suggested velocity response in Fig. 11. These results confirm the change in bulk stiffness expected in the undeformed specimen and suggest the EBSD data in the rolled specimens have primarily been captured on prior-β grains with small angular variations. This succinctly demonstrates the acoustic variations observed with varying propagation angle is due to changes in stiffness anisotropy between prior-β grains.

By taking the elastic constants of titanium from literature for the α- and β-phase, given in Table 2, it is possible to calculate the expected velocity distribution for both phases, shown in Fig. 12(a). Comparing the measured distributions 12 (a) to the modelled velocities 12 (b) and (c) for each phase suggest that measured velocities match well with the expected distribution for pure α, with all specimens exhibiting a peak value within 50 ms^{-1} of the modelled mean of peak. If there was significant influence from the presence of the retained β-phase a velocity

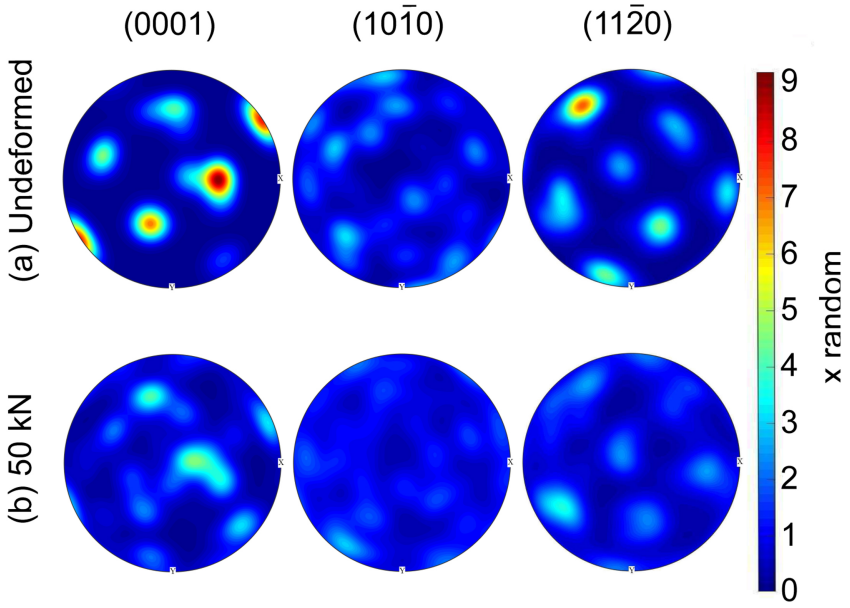

Fig. 9. Pole figure orientation maps of EBSD measured hexagonal α-phase in (a) undeformed and (b) 50 kN rolled specimens in *x*–*z* side-walls. Pole figures are generated from small area EBSD maps.

shift towards 2500 ms^{-1} (the peak β-phase value), would be expected, as the retained β-phase is known to agglomerate at grain boundaries, the shift in peak of 50 ms^{-1} value seen from the undeformed to the 75 kN rolled specimen, is the effect of a greater number of grain boundary crossings, causing the β-phase to have a greater impact of the measured SAW velocity. In Fig. 12(b) the full range of possible α-phase velocity measurements is compared to the expected velocity measurement based on the EBSD-measured α-orientation in the undeformed specimen. The expected velocity values match well with the measured range, and demonstrates that velocities towards 2000 ms^{-1} are not measured as the orientations present in this specimen have characteristic acoustic slowness surfaces with velocities in the upper range (2800–3300 ms^{-1}) of the velocity spectrum for Ti–6Al–4V. The expected velocity distribution suggests measured values should occur around 3200 ms^{-1} in greater abundance than measured. This is possibly due to the limited number of angles (3) where measurements have been captured compared to the calculated angles in the theoretical data (180). Fig. 12(d) is a bivariate plot of Euler angles ϕ_1 and Φ, from the measured EBSD in the undeformed specimen. As expected, a limited number of α-phase variants are seen, typical of a β → α phase transition.

Table 2
Elastic constants for titanium, used to predict velocity distribution [35,36].

	C_{11} GPa	C_{12} GPa	C_{13} GPa	C_{33} GPa	C_{44} GPa	ρ kgm^{-3}
α	170	92	70	192	52	4430
β	135	113	–	–	54.9	4430

From Fig. 7(c) it can be seen that the all grains have the [001] direction aligned or close to the *z*-direction axis but the orientation in the *y*-direction is unknown. Looking at the prior-β structure, the top face is fixed to [001] for the fibre, however crystalline direction may still rotate freely in the *x*–*y* plane. This is of particular interest as this is the plane probed by SRAS when investigating the side-wall specimens (the crystal face exposed in the *x*–*z* plane). This suggests the variation in crystallographic response is due to a change in the orientation of the prior-β grain in the *y*-direction, inducing the formation of α-phase variants with a different characteristic slowness surface. Using Burger's orientation relationship, Eq. (1), the twelve unique α-phase variants were calculated for prior-β orientations of [001] and [101] (aligned

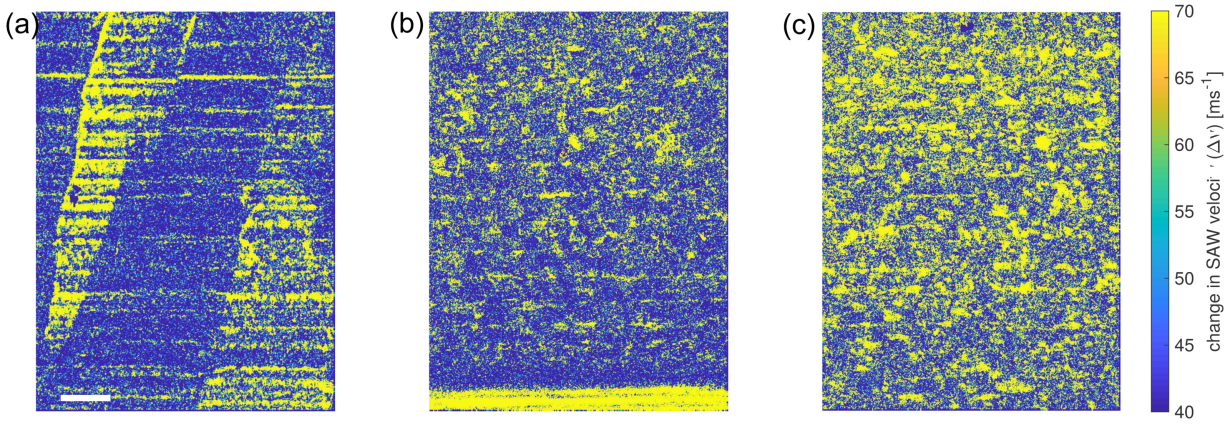

Fig. 10. Contrast mapping of the change in velocity (Δv) at each measurement point between the 0 and 90° propagation direction scans. (a) Undeformed (b) 50 kN rolled and (c) 75 kN rolled. Scale bar shown in (a) indicates 2 mm.

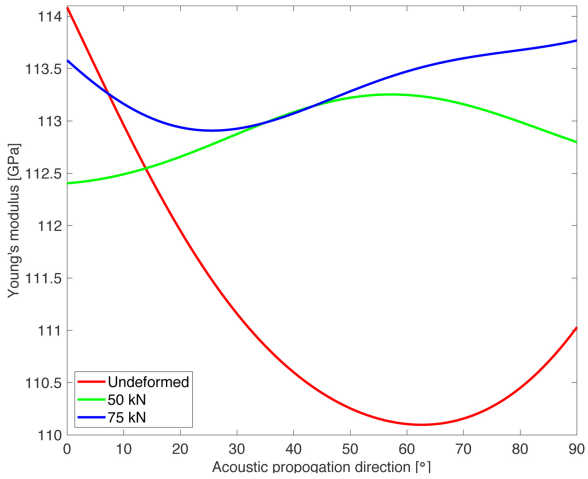

Fig. 11. Young's modulus calculated from EBSD data, using Hill method for tensor averaging. The undeformed specimen shows a significant variance in elasticity with angle, compared to the two rolled specimens. This agrees well with the results presented in Fig. 4. The shift of ~ 4 GPa in the undeformed specimen would correspond to a shift of over 50 ms^{-1} in SAW velocity.

with the *z*-direction). The resulting slowness surfaces for each variant are plotted as a function of propagation angle in Fig. 12(e) and (f). Whilst the twelve variants are calculated, fewer can be seen in the plotted slowness surface; this is due to several orientations being symmetric acoustically. Further to this, there are several orientations pairs which produce slowness surfaces which are exactly 180 degrees out of phase.

The arbitrary mean velocity is shown by the black line for both grains, but in reality this will vary depending upon the exact composition of variants found in the prior-β grain; variant selection is known not to occur evenly [37]. Notably, the [001] orientation shows a measurable shift in velocity between 0 and 45 degrees which matches well with the results of Fig. 4. For grain B however, little to no SAW velocity variation is likely to be measured. Again, the modelled slowness surfaces for grain B match well with the results of Fig. 4, where the larger grains showed little to no SAW velocity variance with propagation angle, in the undeformed specimen. Thus, it can be concluded that the prior-β grains can be detected using SRAS as limited number of possible α-phase variants for a given prior-β orientation lead to large microtextured regions with distinct slowness surfaces. With knowledge of the exact orientation distribution in the region it would be possible to predict the measured slowness surfaces.

4.2. Minimum stiffness direction

One commonly cited issue with strong columnar growth is the directional mechanical properties it bestows upon components. Thus far this has been demonstrated by the change in Young's modulus with angle (Fig. 11). In addition to this it is useful to discuss the extent to which this anisotropy can be detected and characterised by SRAS.

As the material stiffness, E, is proportional to the SAW velocity, SRAS velocity maps captured at multiple propagation directions can be used to indicate the local material anisotropy and stiffness mismatches. Bearing this in mind, regions of measurable velocity gradients, and deviations away from the bulk mean velocity are of interest. Fig. 13(a), plots the maximum change in SAW velocity for the undeformed cross-section (*y*–*z*) specimen. The region in the lower left discussed in Fig. 5 exhibits a maximum change of 300 ms^{-1} in comparison to the bulk, which varies by around 200 ms^{-1}. Interestingly, layer interfaces are clearly indicated in this plot, and suggest a change in velocity of up to 450 ms^{-1}. A similar change is seen in the crown of the deposition; as there has not been the deposition of subsequent layers, recrystallization has not been triggered, indicating initiation of recrystallization is crucial in achieving components with isotropic properties.

The anisotropy information contained within SRAS datasets has also been explored by Mark et al. [38], to indicate the E_{min} direction, where SRAS velocity maps have been captured at multiple propagation angles. This result for the prepared cross-section (*y*–*z*) is shown in Fig. 13(b). For the majority of the specimen there appears to be no clear preferential direction, however for the region in the lower left, there is a clear dominance of angle at or close to 90°. This suggests this region will be highly deformable under loading in the *y*-direction, i.e. though thickness of deposition.

4.3. Extracting build process metrics from acoustic data

It is clear from the acoustic maps that the rolling process is successful in homogenising the specimen microstructure, and this change can be sensed using the SRAS technique. In order to quantify the measured SRAS data, a robust metric must be developed, to relate rolling force effect with acoustic response.

In the unrolled specimen, a clear repetitive banding can be seen in the acoustic map, this can be seen in Fig. 3. These bands are appropriately 1 mm in height and can be correlated to each deposited layer. Martina et al. have previously reported that the α-lamella thickness is known to increase towards the top of a band, due to thermal cycling [21]. This work has recently been expanded by Ho et al. who found this heat affected zone corresponded to coarsening of the lamellar structure, due to transformation coarsening [7]. This variation can be discerned in the acoustic image. Fig. 14 plots the instantaneous the velocity gradient in the *z*-direction. In future, this approach may be used to extract the layer height of deposition for quality control, however this data has been extracted from prepared specimens and further investigations are required to determine if this is feasible on as-deposited specimens.

One of the key aims of this work was to understand how the rolling process affects the acoustic response of the material, and determine if this could be used as a quality control method. In the results presented thus far it is clear that the undeformed specimen can be easily distinguished from the rolled specimens. However, differentiating between the rolled specimens, is not elementary. The large prior-β grains can clearly been seen and sized (Fig. 3), however as the prior-β grain size becomes small and the acoustic variations between grains less distinct sizing of these features becomes difficult. Additionally, for this approach to be viable in-line it would be desirable for the differentiation to be feasibly automated.

A simple automated algorithm was developed in Matlab®, using standard image processing function, as a tool for differentiating between the effects of rolling force. The algorithm is summarised as follows:

- To remove high frequency noise, a Gaussian filter is applied to velocity maps. This has the effect of making only larger features visible. Representative outputs from this stage, for the (a) undeformed and (b) 75 kN rolled specimen, are shown in Fig. 15.
- Taking a nominal location for a seed pixel, the algorithm counts the number of connected pixels which have a measured SAW velocity within 20 ms^{-1}.
- The location of the seed pixel is moved across the specimen.

Fig. 15, shows the distribution of continuous regions within the specimens, as calculated from the algorithm. As expected, the undeformed specimen was characterised by fewer regions in total but typically with a larger size compared to the rolled specimen. Significantly, the algorithm was able to differentiate between the 50 kN and 75 kN rolled specimen. The developed metric is simple and not computationally intensive, potentially making real time processing in-line viable, subject to further development.

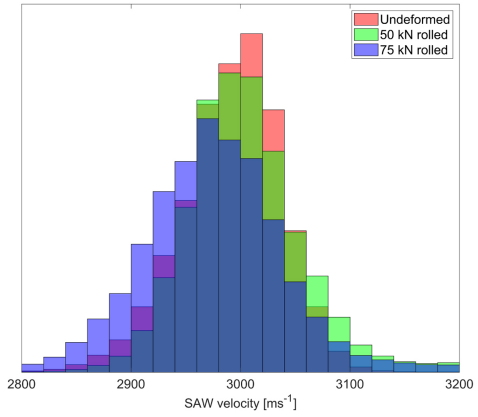

(a)

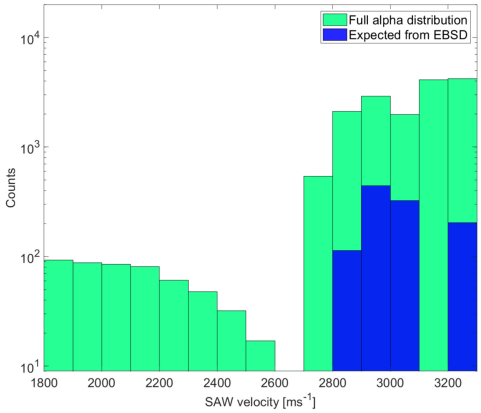

(b)

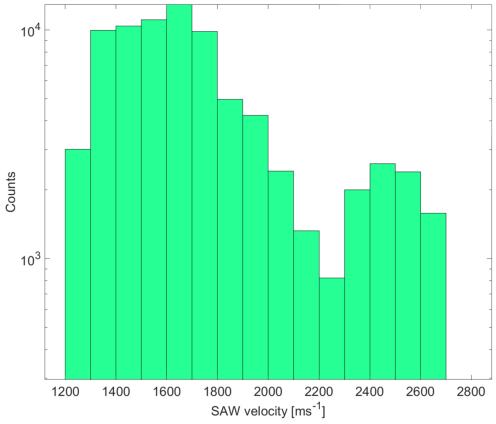

(c)

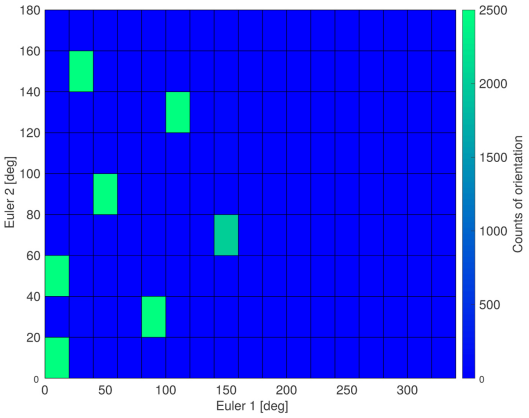

(d)

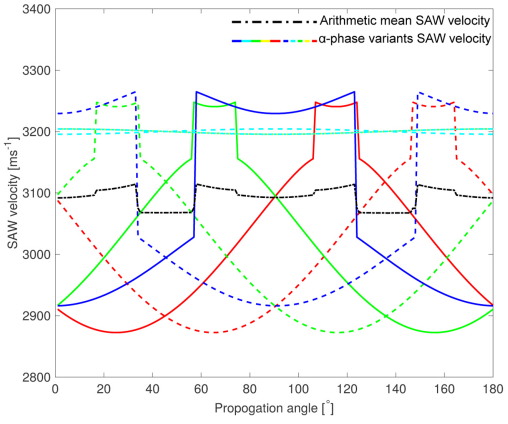

(e)

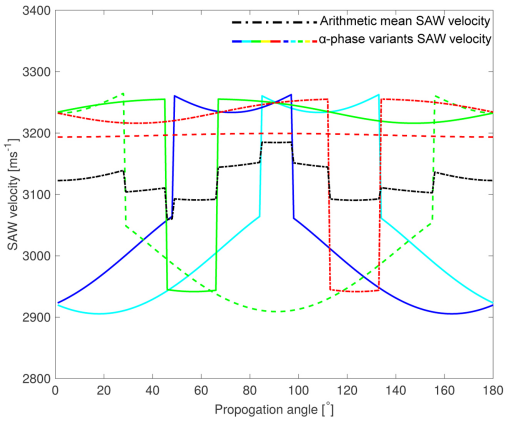

(f)

Fig. 12. Investigation of origin of acoustic response due to texture. (a) Measured velocity distribution for the three side-wall specimens. (b) Comparison of simulated velocity calculated form elastic constant and the predicted velocity distribution, calculated from EBSD measured α-phase orientations. (c) Simulated β-phase. (d) Bivariate plot of Euler angles ϕ_1 and Φ, showing a limited number of orientations, as predicted by the Burgers orientation relationship for one prior-β orientation. (e) Theoretical slowness surfaces for 12 α-phase orientation from prior-β grain with [001] orientation in *y*-direction. (f) Theoretical slowness surfaces for 12 α-phase orientation from prior-β grain with [101] orientation in *y*-direction.

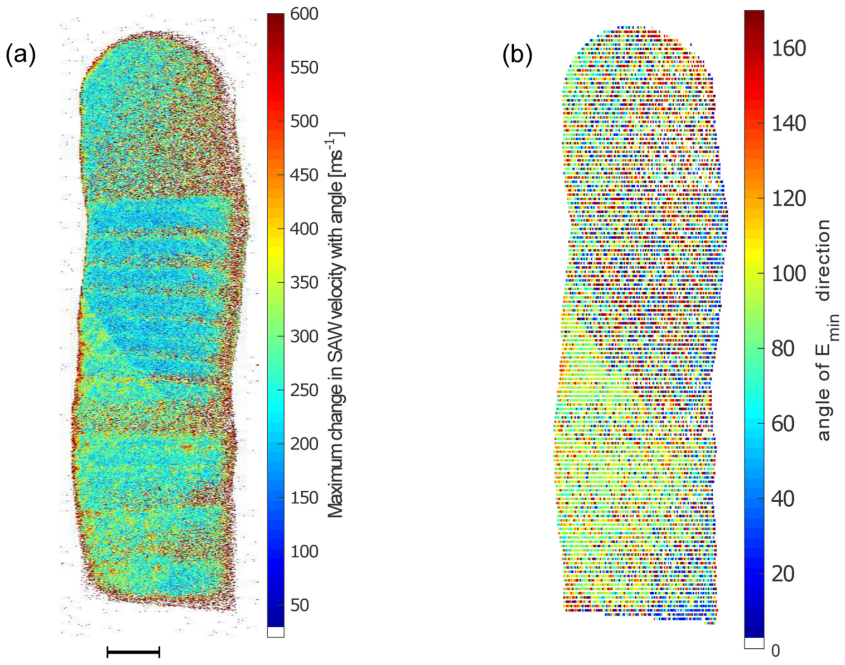

Fig. 13. Prepared cross-section (y–z) of undeformed specimen, (a) plot of maximum change in SAW velocity with varying propagation angle, larger variations indicate more anisotropic behaviour. Scale bar indicates 2 mm. (b) Scatter plot indicating direction of minimum stiffness, E_{min}, relative to the y-direction. Areas with clusters of similar E_{min} directions will be highly deformable under loading.

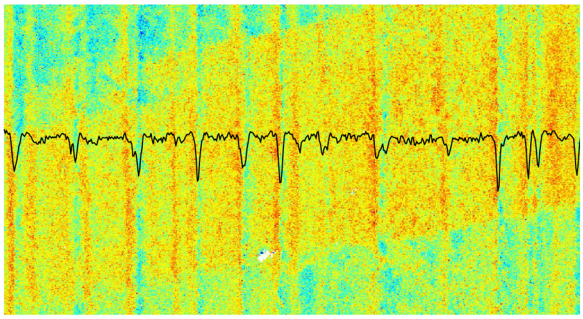

Fig. 14. Extract of effective layer height in deposition from velocity gradient. Example of the response of the layer height algorithm in the undeformed specimen, which calculates the instantaneous velocity gradient in the z-direction (image has been rotated through 90° CW to aid interpretation).

4.4. Industrial solution

All results presented thus far have been captured on prepared specimens, however for the proposed approach of taking measurements in-line and non-destructively for quality control, measurements must be taken from as-deposited surfaces. As-deposited surfaces are optically rough and therefore pose three primary challenges to the use of laser ultrasonics: roughness (out of phase reflections interfere to create a speckle pattern), waviness (drastic changes in the surface normal can mean little light is returned to the detector), and attenuation of the acoustic wave within the material. As SRAS does not rely on time-of-flight measurements, the propagation distance between the generation patch and detection beam can be small to minimise attenuation, allowing the later point to be negated in this work. The use of the normal KED necessitates an optically smooth surface (generally an arithmetic mean roughness, R_a less than 20 nm). Rough surfaces lead to a diffuse reflection of the detection beam and create a speckle pattern from the interference of offset reflections at varying phase. Several techniques exist which can adapt to the speckle patterns that are concomitant with rough surfaces, such as random quadrature demodulation [39], two-wave mixing [40] and the speckle knife edge detector [41]. Other interfeometric techniques such as Fabry–Pérot interferometry, are inherently insensitive to speckle [42]. Use of one such technique, in place of the KED, in the SRAS system would allow the speckle pattern from the rough surface to be efficiently detected. The waviness of the specimens causes two issues, illustrated in Fig. 16, firstly as the height of the deposition varies the detection beam will move out of focus meaning the spot imaged on to the specimen is of larger diameter. Detection efficiency is maximised when $D_{detection} = \lambda_g/4$. Furthermore, the curvature means the beam is no longer perpendicular to the surface, causing the reflected beam to miss the detector.

Patel et al. have recently reported on the use of a speckle knife edge detector to allow SRAS velocity maps to be captured on as-deposited powder-bed AM specimen surfaces [43]. A set-up similar to that used in Patel's experiment has been utilised in this study to explore the possibility and adequacy of imaging on as-deposited WAAM specimens. Clearly, the cross-section is not available for inspection during deposition, thus the side-wall face is more appropriate for discussing as a realistic on-line solution. Fig. 17 shows a SRAS velocity map captured on the as-deposited side-wall in the undeformed specimen. Grey areas in this figure indicate signal drop-out, acoustic waves are propagated parallel to the z-direction. The measured velocity falls within the expected bounds for Ti–6Al–4V, and importantly an outline can be discerned which likely corresponds to a prior-β grain boundary.

Micrographs of the as-deposited surface are shown in Fig. 18 (b) undeformed and (d) 75 kN rolled. A protective oxide layer of varying thickness is distinguished by the varying colour across the undeformed specimen. Furthermore, a prior-β grain boundary can be seen to run across the specimen. Extracted surface profiles for both specimens are shown in Fig. 18(b). Both specimens exhibit a regular periodicity of approximately 1 mm, that can be correlated to the layer height of deposition, with a change in height up to 20 μm. Whilst the undeformed specimen presents little roughness within layers, the rolled specimen repeating striations were seen to develop within the layers from the rolling process. This effect is observed in the surface profile map as the increase in high frequency roughness.

Comparing the velocity map in Fig. 17 to the surface profiles in Fig. 18(a), suggests the rough surface detector is able to cope well with the high frequency roughness but is thwarted by the low frequency waviness, corresponding to build layer periodicity. This topographical variation causes deviations in the position of the returned detection beam which are orders of magnitude larger than that caused by surface roughness. The possible prior-β grain boundary observed in the

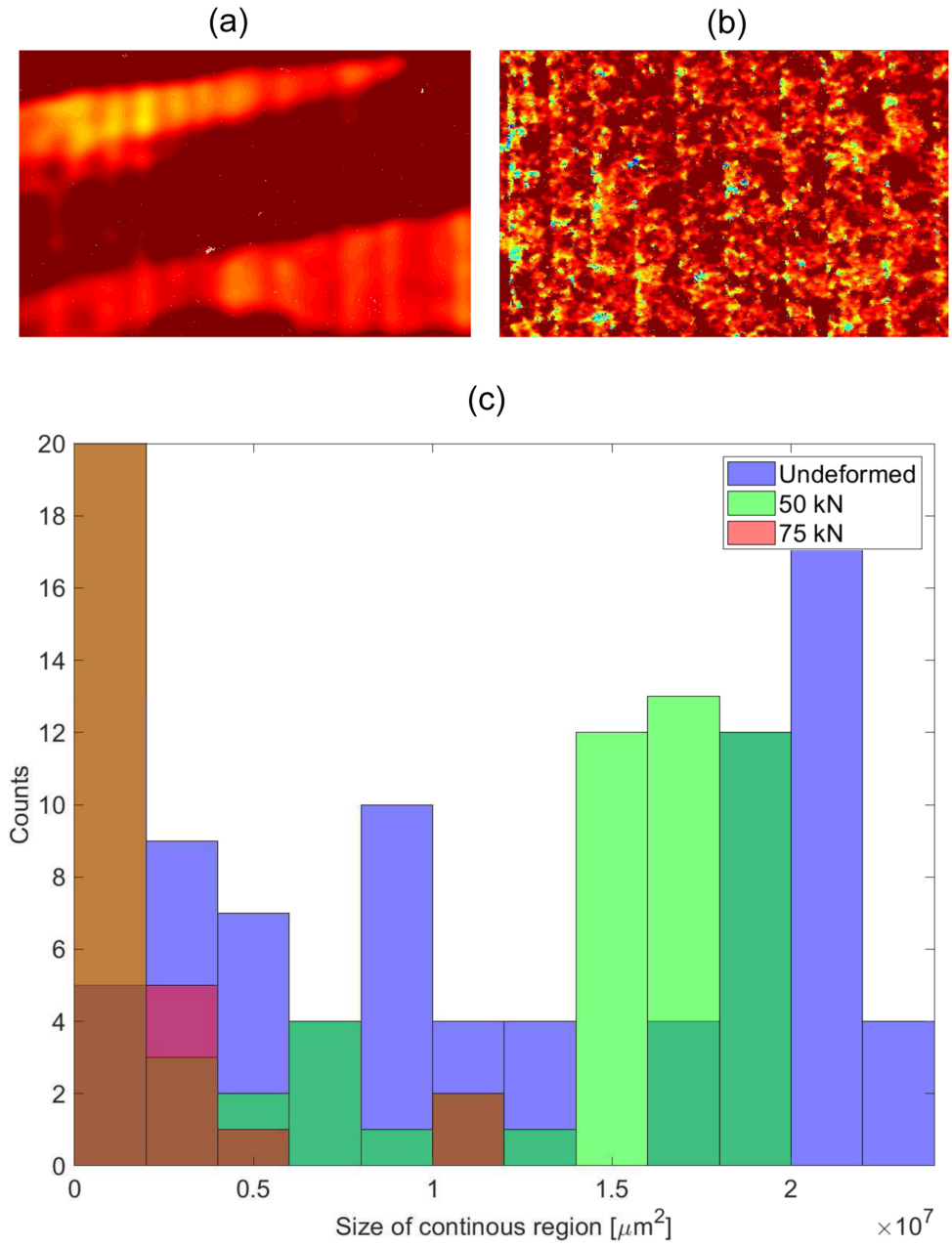

Fig. 15. Representative outputs from algorithm after Gaussian filter has been applied to remove high frequency noise, making detection of larger features such as prior − β feasible for the (a) undeformed and (b) 75 kN rolled specimen. The contrasting feature size is clear to see. (c) RGB Histograms from the three prepared side-wall (x–z) specimens, showing the distribution of continuous regions areal size, as calculated by the developed algorithm.

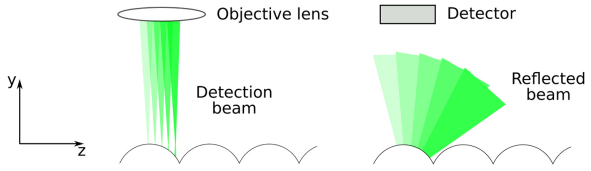

Fig. 16. Schematic optical detection on a surface that is both rough and wavy, as found in the side-wall of WAAM depositions. As the detection beam is scanned along the z-axis the beam moves out of focus due to the change in height of the specimen. This reduces detection efficiency. The rough surface creates a diffuse reflection, visualised as a cone of light, this necessitates the use of a 'rough surface detector'. Furthermore, the curvature of the specimen also changes the surface normal as the beam is scanned, in extreme cases this can mean almost no light is returned to the detector.

undeformed velocity map, compares well with the grain boundary observed in the optical image.

The results presented in Fig. 18(a) show the current ability to capture velocity information on as-deposited surfaces. As expected, the signal degrades due to the deflection of the detection beam from the surface profile, as shown in Fig. 16. In practice it would be possible to employ some form of contour following, allowing the detector system position to be adjusted to maintain a normal to the inspected surface and maintain the correct focal length. However, despite the significant loss of signal in the as-deposited datasets, the information captured is sufficient to still clearly distinguish the unrolled specimen from the rolled specimen. Whilst there is a significant drop-out due to specimen waviness, the result shown in Fig. 18(a) suggests that the macro features can still be seen without the need to scan the full area.

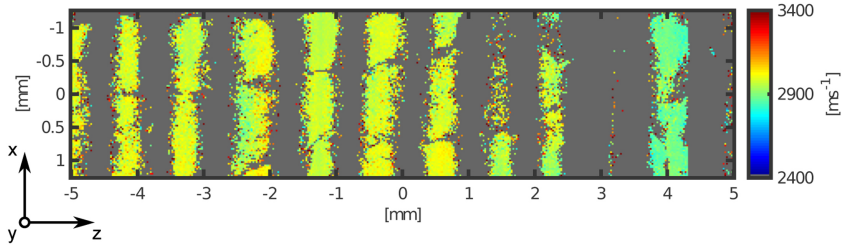

Fig. 17. SRAS velocity map captured from as-deposited side-wall using rough surface detector.

Additionally, measurements may not be feasible during the period where the deposited layer cools, due to both the on-going phase change from a primarily β microstructure to primarily α and the change in temperature altering the elastic modulus and subsequent velocity measurement from the specimen. With the benefit of accurate temperature measurement in the deposit these effects could be decoupled from the SAW velocity, however in order to make meaningful measurements capturing the effect of the rolling process measurement shall be made at room temperature (rolling is applied after each layer of deposition has cooled to ambient). In practice, this avoids the complexities of measuring specimens with a temperature gradient or undergoing phase-change.

Finally, for SRAS to be considered a realistic solution for in-line monitoring the speed of measurement must be considered with respect to the build rate. The WAAM equipment used in this study deposits at a horizontal travel rate of 270 mm min^{-1}. If the primary aim of the in-line inspection system is to decide if rolling has enacted grain refinement, then the step size between measurement points can be large given the width of prior-β grains in the undeformed specimen, 2–6 mm in width. The WAAM system takes around 0.45 s to deposit 2 mm therefore a SRAS system should be able to capture acoustic data in an area (horizontal and vertical) sufficiently large as to identify undeformed prior-β grains in this time. The current SRAS instrumentation can capture ~ 2000 points per second, limited by the generation laser repetition rate, thus in this time it would be possible to capture 900 unique acoustic data points. At an acoustic resolution of 100 μm in both axes, an area of 20 × 45 points or 2 × 4.5 mm could be interrogated; this would sufficiently capture the acoustic response to identify large prior-β grains, whilst keeping pace with the deposition process. Thus, from a practical standpoint there is clearly a good opportunity to integrate SRAS in-line without affecting the fabrication process.

5. Conclusions

The process of inter-pass rolling has previously been shown to drastically improve the functional mechanical properties of components manufactured using the WAAM process. By mapping the texture of WAAM components, through the generation and detection of surface acoustic waves, SRAS scan be used to probe the changes in texture. This work constitutes a primary step towards a viable quality control tool, requisite to the development of WAAM as an industrial solution.

Specifically, this work has demonstrated:

1 The ability of SRAS to detect grain refinement in both side-wall and cross-section WAAM specimens, allowing the differentiation between undeformed and rolled specimens.
2 For the first time SRAS has been utilised on a dual-phase material. It has been shown inherited texturing from the parent β-phase to the child α phase leads to regions with distinct slowness surfaces which can be correlated to prior-β grain growth.
3 Variations in measured acoustic wave velocity with varying propagation angle have been shown to compare well with the Young's

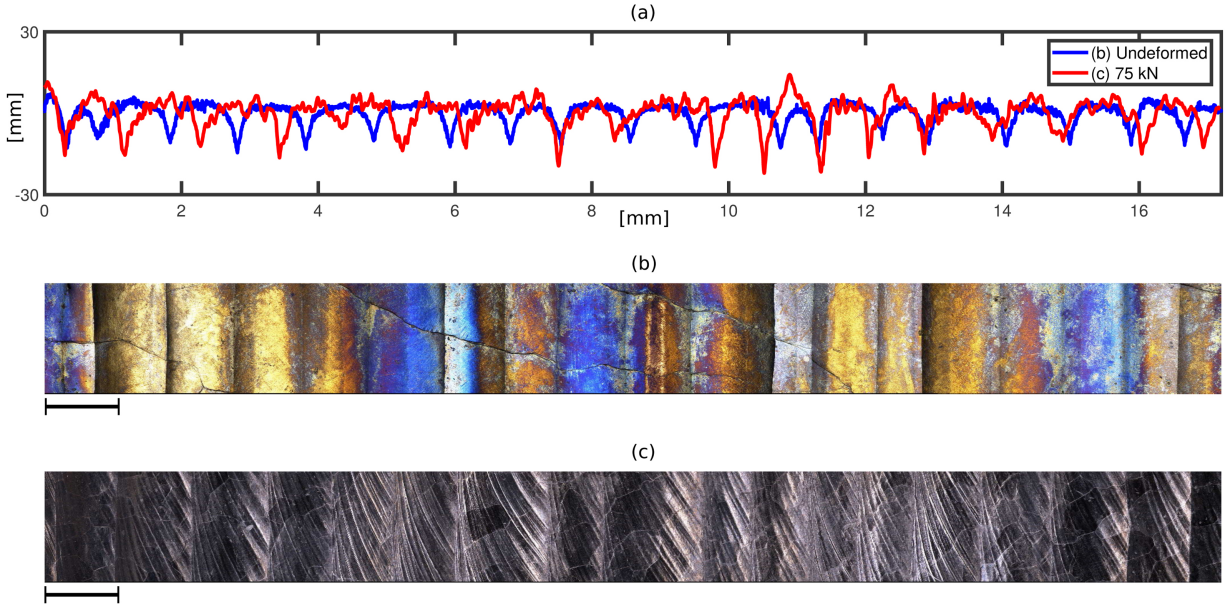

Fig. 18. (a) Line plots of surface topology in as-deposited undeformed and 75 kN rolled specimens. Data plotted in (a) is extracted from high resolution optical microscopy images shown in (b) undeformed and (c) 75 kN rolled, captured using focus variation microscopy. (b) Changes in colour due to varying oxide thickness. A prior-β grain can be seen to run across the specimen. Scale bars indicate 2 mm.

modulus extracted from averaged elasticity tensors, and are indicative of material anisotropy.

4 Further useful build information, such as the minimum stiffness direction and demonstration of strong crystallographic alignment in the substrate can be obtained using SRAS.

5 The development of a metric which allows direct correlation between rolling force and the acoustic response, by measuring the size of distinct regions. This was shown to differentiate between the effect of varying rolling force, as well as undeformed and rolled more generally. This should prove to be fundamental tool for allowing close-loop control from an in-line system.

6 The rates of deposition seen in WAAM pair well with the acquisition speeds a theoretical in-line SRAS system would be capable of. Identification of large prior-β grains would be possible, without impact on the rate of manufacture.

7 A preliminary demonstration of the capability of a 'rough' surface detector system to unravel the speckle pattern, allowing acoustic images to be captured on an as-deposited WAAM surface. This addresses many of the practical difficulties of taking such measurements in-line.

Future reporting should focus on the design and instrumentation of an appropriate system for real-time inspection, and further thorough investigations on as-deposited surface imaging.

Acknowledgements

This work was supported by the Engineering and Physical Sciences Research Council [grant numbers EP/K029010/1 and EP/L022125/1]. All authors have no conflict of interest to report. The authors thank Michael Draper at Intertek Metallurgy Lab for assistance in metallographic preparation, and The Nanoscale and Microscale Research Centre (nmRC) at The University of Nottingham for the SEM and OM equipment, and EBSD software. Additionally, Alistair Speidel is thanked for his assistance acquiring focus variation microscopy images.

References

[1] P. Almeida, S. Williams, Innovative process model of Ti?6Al ?4V additive layer manufacturing using cold metal transfer (CMT), Innovative process model of Ti?6Al ?4V additive layer manufacturing using cold metal transfer (CMT), 21st Solid Freeform Fabrication Symposium, 21st Solid Freeform Fabrication Symposium (2010), https://pdfs.semanticscholar.org/2b35/4c12606e90425b1613b5dc475807f89668d5.pdf.

[2] F. Martina, J. Mehnen, S.W. Williams, P. Colegrove, F. Wang, Investigation of the benefits of plasma deposition for the additive layer manufacture of Ti–6Al–4V, J. Mater. Process. Technol. 212 (6) (2012) 1377–1386, https://doi.org/10.1016/j.jmatprotec.2012.02.002.

[3] F. Martina, J. Ding, S. Williams, A. Caballero, G. Pardal, L. Quintino, Tandem metal inert gas process for high productivity wire arc additive manufacturing in stainless steel, Addit. Manuf. 25 (2019) 545–550, https://doi.org/10.1016/j.addma.2018.11.022.

[4] S.W. Williams, F. Martina, A.C. Addison, J. Ding, G. Pardal, P. Colegrove, Wire + arc additive manufacturing, Mater. Sci. Technol. 32 (7) (2016) 641–647, https://doi.org/10.1179/1743284715Y.0000000073.

[5] M.J. Donachie, Titanium: A Technical Guide, 2nd ed., ASM International, 2000.

[6] F. Wang, S. Williams, P. Colegrove, A.A. Antonysamy, Microstructure and mechanical properties of wire and arc additive manufactured Ti–6Al–4V, Metall. Mater. Trans. A 44 (2) (2013) 968–977, https://doi.org/10.1007/s11661-012-1444-6.

[7] A. Ho, H. Zhao, J.W. Fellowes, F. Martina, A.E. Davis, P.B. Prangnell, On the origin of microstructural banding in Ti–6Al–4V wire–arc based high deposition rate additive manufacturing, Acta Mater. 166 (2019) 306–323, https://doi.org/10.1016/j.actamat.2018.12.038.

[8] L. Germain, S.R. Dey, M. Humbert, N. Gey, Determination of parent orientation maps in advanced titanium-based alloys, J. Microsc. 227 (3) (2007) 284–291.

[9] P. Davies, An Investigation of Microstructure and Texture Evolution in the Near-alpha Titanium Alloy Ti Metal 834, Ph.D. thesis, University of Sheffield, 2009.

[10] M. Humbert, F. Wagner, C. Esling, Numbering the crystallographic variants in phase transformation, J. Appl. Cryst. 25 (6) (1992) 724–730, https://doi.org/10.1107/S0021889892005375.

[11] F. Dunne, A. Walker, D. Rugg, A systematic study of hcp crystal orientation and morphology effects in polycrystal deformation and fatigue, Proc. R. Soc. Lond. A: Math. Phys. Eng. Sci. 463 (2082) (2007) 1467–1489, https://doi.org/10.1098/rspa.2007.1833.

[12] V. Sinha, M. Mills, J.C. Williams, J. Spowart, Observations on the faceted initiation site in the dwell-fatigue tested Ti-6242 alloy: crystallographic orientation and size effects, Metallur. Mater. Trans. A 37 (5) (2006) 1507–1518, https://doi.org/10.1007/s11661-006-0095-x.

[13] W.E. Frazier, Metal additive manufacturing: A review, J. Mater. Eng. Perform. 23 (2014), https://doi.org/10.1007/s11665-014-0958-z.

[14] J. Donoghue, A. Antonysamy, F. Martina, P.A. Colegrove, S. Williams, P. Prangnell, The effectiveness of combining rolling deformation with wire–arc additive manufacture on beta-grain refinement and texture modification in Ti–6Al–4V, Mater. Charact. 114 (2016) 103–114, https://doi.org/10.1016/j.matchar.2016.02.001.

[15] M. Simonelli, Y. Tse, C. Tuck, Effect of the build orientation on the mechanical properties and fracture modes of SLM Ti–6Al–4V, Mater. Sci. Eng.: A 616 (2014) 1–11, https://doi.org/10.1016/j.msea.2014.07.086.

[16] I. Bantounas, D. Dye, T.C. Lindley, The role of microtexture on the faceted fracture morphology in Ti–6Al–4V subjected to high-cycle fatigue, Acta Mater. 58 (11) (2010) 3908–3918, https://doi.org/10.1016/j.actamat.2010.03.036.

[17] B.E. Carroll, T.A. Palmer, A.M. Beese, Anisotropic tensile behavior of Ti–6Al–4V components fabricated with directed energy deposition additive manufacturing, Acta Mater. 87 (2015) 309–320, https://doi.org/10.1016/j.actamat.2014.12.054.

[18] J.H. Martin, B.D. Yahata, J.M. Hundley, J.A. Mayer, T.A. Schaedler, T.M. Pollock, 3d printing of high-strength aluminium alloys, Nature 549 (2017) 365–369, https://doi.org/10.1038/nature23894.

[19] P.A. Colegrove, H.E. Coules, J. Fairman, F. Martina, T. Kashoob, H. Mamash, L.D. Cozzolino, Microstructure and residual stress improvement in wire and arc additively manufactured parts through high-pressure rolling, J. Mater. Process. Technol. 213 (10) (2013) 1782–1791, https://doi.org/10.1016/j.jmatprotec.2013.04.012.

[20] P.A. Colegrove, F. Martina, M.J. Roy, B.A. Szost, S. Terzi, S.W. Williams, P.J. Withers, D. Jarvis, High pressure interpass rolling of wire+ arc additively manufactured titanium components, in: Advanced Materials Research, Vol. 996, Trans Tech Publ., 2014, pp. 694–700, , https://doi.org/10.4028/www.scientific.net/AMR.996.694.

[21] F. Martina, P.A. Colegrove, S.W. Williams, J. Meyer, Microstructure of interpass rolled wire + arc additive manufacturing Ti–6Al–4V components, Metallur. Mater. Trans. A 46 (12) (2015) 6103–6118, https://doi.org/10.1007/s11661-015-3172-1.

[22] T. Caffrey, I. Campbell, T. Wohlers, Wohlers Report 2016: Additive Manufacturing and 3D Printing State of the Industry, Annual Worldwide Progress Report, Wohlers Associates, Inc, Fort Collins, 2016.

[23] S.K. Everton, M. Hirsch, P. Stravroulakis, R.K. Leach, A.T. Clare, Review of in-situ process monitoring and in-situ metrology for metal additive manufacturing, Mater. Des. (2016), https://doi.org/10.1016/j.matdes.2016.01.099.

[24] A.R. McAndrew, M. Alvarez Rosales, P.A. Colegrove, J.R. Honnige, A. Ho, R. Fayolle, K. Eyitayo, I. Stan, P. Sukrongpang, A. Crochemore, Z. Pinter, Interpass rolling of Ti–6Al–4V wire + arc additively manufactured features for microstructural refinement, Addit. Manuf. 21 (2018) 340–349, https://doi.org/10.1016/j.addma.2018.03.006.

[25] W. Li, S.D. Sharples, R.J. Smith, M. Clark, M.G. Somekh, Determination of crystallographic orientation of large grain metals with surface acoustic waves, J. Acoust. Soc. Am. 132 (2) (2012) 738–745, https://doi.org/10.1121/1.4731226.

[26] R.J. Smith, W. Li, J. Coulson, M. Clark, M.G. Somekh, S.D. Sharples, Spatially resolved acoustic spectroscopy for rapid imaging of material microstructure and grain orientation, Meas. Sci. Technol. 25 (5) (2014) 055902, https://doi.org/10.1088/0957-0233/25/5/055902.

[27] G.W. Farnell, Properties of Elastic Surface Waves (Physical Acoustics), vol. 6, Academic, New York, 1970.

[28] R.J. Smith, M. Hirsch, R. Patel, W. Li, A.T. Clare, S.D. Sharples, Spatially resolved acoustic spectroscopy for selective laser melting, J. Mater. Process. Technol. 236 (2016) 93–102, https://doi.org/10.1016/j.jmatprotec.2016.05.005.

[29] M. Hirsch, S. Catchpole-Smith, R. Patel, P. Marrow, W. Li, C. Tuck, S.D. Sharples, A.T. Clare, Meso-scale defect evaluation of selective laser melting using spatially resolved acoustic spectroscopy, Proc. R. Soc. Lond. A: Math., Phys. Eng. Sci. 473 (2005), https://doi.org/10.1098/rspa.2017.0194.

[30] M. Hirsch, P. Dryburgh, S. Catchpole-Smith, R. Patel, L. Parry, S. Sharples, I. Ashcroft, A. Clare, Targeted rework strategies for powder bed additive manufacture, Addit. Manuf. 19 (2018) 127–133, https://doi.org/10.1016/j.addma.2017.11.011.

[31] F. Martina, Investigation of Methods to Manipulate Geometry, Microstructure and Mechanical Properties in Titanium Large Scale Wire + Arc Additive Manufacturing, Ph.D. thesis, Cranfield University, 2014.

[32] W. Li, J. Coulson, P. Marrow, R.J. Smith, S.J. Lainé, M. Clark, S.D. Sharples, Crystallographic orientation determination of hexagonal structure crystals by laser ultrasonic technique, J. Phys.: Conf. Ser. 684 (1) (2016) 012001, https://doi.org/10.1088/1742-6596/684/1/012001.

[33] C.M. Kube, J.A. Turner, Voigt, Reuss, Hill, and self-consistent techniques for modeling ultrasonic scattering, 41, st Annual Review of Progress in Quantitative Nondestructive Evaluation (QNDE) (2015), https://doi.org/10.1063/1.4914698.

[34] R. Acharya, S. Das, Additive manufacturing of IN100 superalloy through scanning laser epitaxy for turbine engine hot-section component repair: process development, modeling, microstructural characterization, and process control, Metallur. Mater. Trans. A 46 (9) (2015) 3864–3875, https://doi.org/10.1007/s11661-015-2912-6.

[35] J. Warwick, J. Coakley, S. Raghunathan, R. Talling, D. Dye, Effect of texture on load partitioning in Ti–6Al–4V, Acta Mater. 60 (2012) 4117–4127, https://doi.org/10.1016/j.actamat.2012.03.039.

[36] J. Bernier, J.-S. Park, A. Pilchak, M. Glavicic, M. Miller, Measuring stress distributions in Ti–6Al–4V using synchrotron X-ray diffraction, Metallur. Mater. Trans. A 39 (13) (2008) 3120–3133, https://doi.org/10.1007/s11661-008-9639-6.

[37] D. Qiu, R. Shi, D. Zhang, W. Lu, Y. Wang, Variant selection by dislocations during alpha precipitation in alpha/beta titanium alloys, Acta Mater. 88 (2015) 218–231, https://doi.org/10.1016/j.actamat.2014.12.044.

[38] A. Mark, W. Li, S.D. Sharples, P.J. Withers, Comparison of grain to grain orientation

and stiffness mapping by spatially resolved acoustic spectroscopy and EBSD, J. Microsc. 627 (1) (2017) 89–97, https://doi.org/10.1111/jmi.12550.
[39] B. Pouet, S. Breugnot, P. Clemenceau, Robust laser ultrasonic interferometer based on random quadrature demodulation, in: AIP Conference Proceedings, Vol. 820, AIP (2006) 233–239, https://doi.org/10.1063/1.2184534.
[40] J. Ke, C. Duan, W. Yi, C. Yan, Application of an adaptive two-wave mixing interferometer for detection of surface defects, in: 2016 Progress in Electromagnetic Research Symposium (PIERS) (2016) 2142–2146, https://doi.org/10.1109/piers.2016.7734892.
[41] S.D. Sharples, R.A. Light, S.O. Achamfuo-Yeboah, M. Clark, M.G. Somekh, The SKED: speckle knife edge detector, J. Phys.: Conf. Ser. 520 (2014) 012004, https://doi.org/10.1088/1742-6596/520/1/012004.
[42] I. Bogatyreva, V. Dan'ilchenko, L. Pospelov, Theory of Fabry–Perot interferometer with statistically rough mirrors, Radiophys. Quantum Electron. 26 (1) (1983) 49–54, https://doi.org/10.1007/BF01038774.
[43] R. Patel, M. Hirsch, P. Dryburgh, D. Pieris, S. Achamfuo-Yeboah, R. Smith, R. Light, S. Sharples, A. Clare, M. Clark, Imaging material texture of as-deposited selective laser melted parts using spatially resolved acoustic spectroscopy, Appl. Sci. 8 (10) (2018) 1991, https://doi.org/10.3390/app8101991.

2019-05-15

Spatially resolved acoustic spectroscopy for integrity assessment in wire-arc additive manufacturing

Dryburgh, Paul

Elsevier

Dryburgh P, Pieris D, Martina F, et al., Spatially resolved acoustic spectroscopy for integrity assessment in wire-arc additive manufacturing. Additive Manufacturing, Volume 28, August 2019, pp. 236-251

https://doi.org/10.1016/j.addma.2019.04.015